The Astrophysical Journal Supplement Series, 262:14 (31pp), 2022 September https://doi.org/10.3847/1538-4365/ac7beb

Monitoring AGNs with Hβ Asymmetry. III. Long-term Reverberation Mapping Results of 15 Palomar–Green Quasars

Dong-Wei Bao[1,2], Michael S. Brotherton[3], Pu Du[1], Jacob N. McLane[3], T. E. Zastrocky[3,4], Kianna A. Olson[3], Feng-Na Fang[1,2], Shuo Zhai[1,2], Zheng-Peng Huang[1], Kai Wang[1], Bi-Xuan Zhao[5], Sha-Sha Li[6], Sen Yang[1,2], Yong-Jie Chen[1,2], Jun-Rong Liu[1,2], Zhu-Heng Yao[1,2], Yue-Chang Peng[1,2], Wei-Jian Guo[1,2], Yu-Yang Songsheng[1,2], Yan-Rong Li[1], Bo-Wei Jiang[1,2], David H. Kasper[3], William T. Chick[3], My L. Nguyen[3], Jaya Maithil[3], H. A. Kobulnicky[3], D. A. Dale[3], Derek Hand[3], C. Adelman[3,7], Z. Carter[3,8], A. M. Murphree[3,9], M. Oeur[3,10], S. Schonsberg[3,11], T. Roth[3,12], Hartmut Winkler[13], Paola Marziani[14], Mauro D'Onofrio[15], Chen Hu[1], Ming Xiao[1], Suijian Xue[16], Bożena Czerny[17], Jesús Aceituno[18,19], Luis C. Ho[20,21], Jin-Ming Bai[6], and Jian-Min Wang[1,2,22,23]

(MAHA Collaboration)

[1] Key Laboratory for Particle Astrophysics, Institute of High Energy Physics, Chinese Academy of Sciences, 19B Yuquan Road, Beijing 100049, People's Republic of China; dupu@ihep.ac.cn
[2] School of Astronomy and Space Science, University of Chinese Academy of Sciences, 19A Yuquan Road, Beijing 100049, People's Republic of China
[3] Department of Physics and Astronomy, University of Wyoming, Laramie, WY 82071, USA; mbrother@uwyo.edu
[4] Physics and Astronomy Department, Regis University, Denver, CO 80212, USA
[5] Shanghai Observatory, Chinese Academy of Sciences, 80 Nandan Road, Shanghai 200030, People's Republic of China
[6] Yunnan Observatories, Chinese Academy of Sciences, Kunming 650011, People's Republic of China
[7] Department of Physics & Astronomy, Cal Poly Pomona, Pomona, CA 91768, USA
[8] Department of Physics and Astronomy, Trinity University, San Antonio, TX 78212, USA
[9] Department of Physics, Rhodes College, Memphis, TN 38112, USA
[10] Department of Physics and Astronomy, State Long Beach, Long Beach, CA 90840, USA
[11] Department of Physics and Astronomy, University of Montana, Missoula, MT 59812, USA
[12] Department of Physics & Astronomy, California State University, Sacramento, CA 95747, USA
[13] Department of Physics, University of Johannesburg, P.O. Box 524, 2006 Auckland Park, South Africa
[14] Istituto Nazionale di Astrofisica (INAF), Osservatorio Astronomico di Padova, I-35122 Padova, Italy
[15] Dipartimento di Fisica & Astronomia "Galileo Galilei", Università di Padova, Padova, Italy
[16] Key Laboratory of Optical Astronomy, National Astronomical Observatories, Chinese Academy of Sciences, Beijing 100012, People's Republic of China
[17] Center for Theoretical Physics, Polish Academy of Sciences, Al. Lotnikow 32/46, 02-668 Warsaw, Poland
[18] Centro Astronomico Hispano Alemán, Sierra de los filabres sn, E-04550 Gergal, Almería, Spain
[19] Instituto de Astrofísica de Andalucía (CSIC), Glorieta de la astronomía sn, E-18008 Granada, Spain
[20] Kavli Institute for Astronomy and Astrophysics, Peking University, Beijing 100871, People's Republic of China
[21] Department of Astronomy, School of Physics, Peking University, Beijing 100871, People's Republic of China
[22] National Astronomical Observatories of China, Chinese Academy of Sciences, 20A Datun Road, Beijing 100020, People's Republic of China
Received 2022 March 16; revised 2022 June 7; accepted 2022 June 22; published 2022 August 22

Abstract

In this third paper of the series reporting on the reverberation mapping campaign of active galactic nuclei with asymmetric Hβ emission-line profiles, we present results for 15 Palomar–Green quasars using spectra obtained between the end of 2016–2021 May. This campaign combines long time spans with relatively high cadence. For eight objects, both the time lags obtained from the entire light curves and the measurements from individual observing seasons are provided. Reverberation mapping of nine of our targets has been attempted for the first time, while the results for six others can be compared with previous campaigns. We measure the Hβ time lags over periods of years and estimate their black hole masses. The long duration of the campaign enables us to investigate their broad-line region (BLR) geometry and kinematics for different years by using velocity-resolved lags, which demonstrate signatures of diverse BLR geometry and kinematics. The BLR geometry and kinematics of individual objects are discussed. In this sample, the BLR kinematics of Keplerian/virialized motion and inflow is more common than that of outflow.

Unified Astronomy Thesaurus concepts: Reverberation mapping (2019); Active galactic nuclei (16); Active galaxies (17); Supermassive black holes (1663); Quasars (1319)

Supporting material: machine-readable tables

1. Introduction

The broad emission lines of active galactic nuclei (AGNs), are the primary features in their UV/optical spectra and arise from the photoionization of gas in the broad-line regions (BLRs) by the continuum emission from the accretion disks around the central supermassive black holes (SMBHs). Although the profiles of the broad Balmer emission lines (e.g., Hα, Hβ, Hγ) in AGNs are sometimes well approximated by Gaussian or Lorentzian functions, a fraction of them are more complex and possess

[23] PI of the MAHA Project.

significant asymmetries (redward, blueward, or double-peaked) sometimes with systematic velocity shifts of their peaks (e.g., De Robertis 1985; Sulentic 1989; Marziani et al. 2003a; Eracleous et al. 2012). The physical origin of the profile asymmetries of broad emission lines is far from fully understood, but it is likely that the asymmetries are connected with the kinematics of BLRs or opacity effects.

In past decades, observational studies often focused on emission-line profiles and their correlations with other AGN properties. For example, Boroson & Green (1992) discovered that the Hβ profile tends to be red asymmetric if the Fe II emissions are weak and the [O III] lines are strong (the main variations in the so-called Eigenvector 1). Marziani et al. (2003b) divided a sample of AGNs into several bins with different black hole (BH) masses and Eddington ratios and investigated the systematic properties of the median profiles of broad Hβ in each bin, showing that redward asymmetries are observed at a low Eddington ratio. Netzer & Trakhtenbrot (2007) studied AGNs from the Sloan Digital Sky Survey (SDSS) and found that the fractional flux of the red part of the Hβ line shows a positive correlation with luminosity and a negative correlation with the flux ratio of Fe II/Hβ. Hu et al. (2008) discovered that the Hβ line shows a more significantly red asymmetry if the Fe II emission lines have stronger redshifted velocities.

Additionally, theoretical efforts were made to understand the diversity of emission-line profiles. Capriotti et al. (1979) proposed that the line asymmetries could be attributed to optically thick inflowing or outflowing BLR clouds. Ferland et al. (1979) calculated asymmetric profiles from an expanding BLR by taking into account Balmer self-absorption of optically thick clouds. Chen et al. (1989) and Chen & Halpern (1989) found that a relativistic Keplerian disk can explain the observed asymmetric and double-peaked profile observed in Arp 102B. Eracleous et al. (1995) suggested that a relativistic eccentric disk could account for observed asymmetries. Storchi-Bergmann et al. (2003) used the spiral arms in a disk to explain the Hα line profile variations of NGC 1097. Wang et al. (2017) suggested that the BLR could be formed through tidal disruption of clumps from a dusty torus, showing asymmetric profiles due to the infall of the captured gas. Asymmetries of profiles generated by this model are generally consistent with profiles of Palomar–Green (PG) quasars. Furthermore, supermassive binary black holes (SMBBHs) were also recently proposed to explain double-peaked profiles (e.g., Shen & Loeb 2010; Bon et al. 2012; Li et al. 2016; Ji et al. 2021).

The reverberation mapping (RM) technique (Blandford & McKee 1982; Peterson 1993) is a powerful tool for investigating the geometry and kinematics of BLRs, by monitoring the delayed response of the broad emission lines with respect to the continuum variation, and has been carried out for more than a hundred AGNs over the past several decades. Before 2000, investigations focused on, for example, bright but heterogeneous samples of Seyfert 1 galaxies (Peterson et al. 1998), PG quasars (Kaspi et al. 2000), or intensive studies of some individual objects (e.g., International AGN Watch project; see Clavel et al. 1991; Peterson et al. 2002). These efforts established a general understanding of the RM properties of AGNs. Since 2000, significant progress has been made by dedicated RM projects with different goals. For example, the Lick AGN Monitoring Project (LAMP; see, e.g., Bentz et al. 2008; Barth et al. 2015; U et al. 2022) resolved the BLR kinematics of some local Seyfert galaxies. The super-Eddington accreting massive black holes (SEAMBHs) project (e.g., Du et al. 2014, 2015, 2016b, 2018b) focuses on the AGNs with the highest accretion rates and found shortened time lags compared to other objects of similar luminosity. Industrial-scale RM campaigns like the SDSS RM project (e.g., Shen et al. 2016; Grier et al. 2017), and the Australian Dark Energy Survey (OzDES) RM program (Yu et al. 2021) use fiber-fed instruments and can obtain the time delays of multiple objects in the field of view simultaneously. Barth et al. (2013) and Hu et al. (2015) measured the time lags of Fe II lines. Rafter et al. (2011) and Woo et al. (2019) monitored intermediate-mass black holes, while Rakshit et al. (2019) and Li et al. (2021) observed luminous nearby quasars (e.g., 5100 Å luminosity $\gtrsim 10^{45}$ erg s^{-1}). Some long-term projects aim to measure C IV or C III] emission lines in high-redshift quasars in a time span of decades (Kaspi et al. 2017, 2021; Lira et al. 2018). There are also many recent campaigns for small samples of (or individual) interesting AGNs (e.g., Denney et al. 2009; Grier et al. 2012; Lu et al. 2016; Fausnaugh et al. 2017; De Rosa et al. 2018; Zhang et al. 2018; Czerny et al. 2019; Hu et al. 2020b; Zajaček et al. 2020, 2021; Oknyansky et al. 2021).

To understand the kinematics associated with the asymmetries of emission-line profiles and to explore the evolution of BLR gas, we initiated a dedicated RM campaign in 2016 named the Monitoring AGNs with Hβ Asymmetry (MAHA) project. We focus on AGNs with asymmetric (or double-peaked) emission lines, which are more likely connected with complicated BLR geometry or kinematics. Another goal of the MAHA project is to search for SMBBH candidates from transfer functions (also called "velocity-delay maps") produced by RM (Wang et al. 2018; Kovačević et al. 2020; Songsheng et al. 2020).

We have previously published the RM results of seven Seyfert galaxies observed from the end of 2016–2017 May (Du et al. 2018a; hereafter Paper I and Brotherton et al. 2020; hereafter Paper II). Some of the objects show very complicated signatures in their velocity-resolved lags (e.g., Ark 120 and Mrk 6) or velocity-delay maps (e.g., Mrk 79), which are difficult to interpret as simple inflow, outflow, or virialized motions (see Papers I and II). The discovery of the diverse BLR kinematics in Seyfert galaxies with asymmetric line profiles (Papers I and II) motivates us to consider whether the BLR geometry and kinematics are also complex in more luminous quasars with asymmetric Hβ.

The PG sample of objects with ultraviolet excesses (Schmidt & Green 1983; Boroson & Green 1992) includes subsamples of quasars that have been extensively studied in almost all wavelengths of the electromagnetic spectrum and some have already been spectroscopically monitored for RM (e.g., Kaspi et al. 2000; Bentz et al. 2009; Grier et al. 2012; Barth et al. 2015; Zhang et al. 2018; Hu et al. 2020a, 2020b). The asymmetries of their emission-line profiles have been investigated using single-epoch spectra (Boroson & Green 1992; Marziani et al. 2003b), but not systematically in the time domain. It is valuable to investigate the geometry and kinematics of their BLRs for the PG quasars with significantly asymmetric emission lines by the velocity-resolved lags (e.g., Bentz et al. 2009; Denney et al. 2010; Du et al. 2016a) or velocity-delay maps (e.g., Grier et al. 2013; Xiao et al. 2018; Horne et al. 2021). As the third paper of the MAHA series, we

Table 1
Basic Information of the 15 PG Targets

Name	Other Names	R.A.	Decl.	z	A	A (Boroson+92)	Observatories	Previous RM
PG 0007+106	Mrk 1501, III Zw 2	00:10:31.0	+10:58:29	0.0872	−0.022	−0.046	WIRO, Asiago, SAAO	(1)
PG 0049+171	Mrk 1148	00:51:54.7	+17:25:59	0.0645	−0.063	−0.047	WIRO	
PG 0923+129	Mrk 705, Ark 202	09:26:03.3	+12:44:03	0.0288	−0.072	−0.031	WIRO	
PG 0947+396		09:50:48.4	+39:26:51	0.2055	−0.116	−0.148	WIRO	
PG 1001+054		10:04:20.1	+05:13:00	0.1601	+0.065	+0.082	Lijiang	
PG 1048+342		10:51:43.8	+33:59:27	0.1671	−0.226	+0.045	WIRO	(2)*
PG 1100+772	3C 249.1	11:04:13.6	+76:58:58	0.3115	−0.106	−0.097	WIRO & Asiago	
PG 1202+281	GQ Com	12:04:42.1	+27:54:12	0.1650	−0.095	−0.298	WIRO & Asiago	
PG 1211+143		12:14:17.6	+14:03:13	0.0809	+0.039	−0.003	Lijiang & CAHA	(2)
PG 1310−108		13:13:05.7	−11:07:42	0.0343	−0.112	−0.075	WIRO	
PG 1351+640		13:53:15.8	+63:45:46	0.0882	−0.139	+0.136	WIRO	(2)*
PG 1351+695	Mrk 279	13:53:03.4	+69:18:29	0.0305	−0.043		WIRO	(3,4,5)
PG 1501+106	Mrk 841	15:04:01.2	+10:26:16	0.0364	−0.071	−0.039	WIRO, Asiago, SAAO	(6)
PG 1534+580	Mrk 290	15:35:52.3	+57:54:09	0.0302	−0.109	+0.044	WIRO	(7)
PG 1613+658	Mrk 876	16:13:57.1	+65:43:10	0.1211	−0.183	−0.207	WIRO	(2,8)

Note. A is a dimensionless parameter to describe the asymmetry, which is measured from our campaign (see Section 2.1). A (Boroson+92) is the asymmetry parameter listed in Boroson & Green (1992). References: (1) Grier et al. (2012), (2) Kaspi et al. (2000), (3) Maoz et al. (1990), (4) Santos-Lleó et al. (2001), (5) Barth et al. (2015), (6) Brotherton et al. (2020), (7) Denney et al. (2010), (8) Minezaki et al. (2019). * means that the previous RM campaign did not successfully measure the time lag of Hβ.

(This table is available in machine-readable form.)

report here the RM observations of 15 PG quasars, most with significantly asymmetric Hβ emission lines.

The paper is organized as follows. The target selection and the observations are given in Section 2. The analyses are provided in Section 3, including the mean and rms spectra, the light curves, the line widths, the time-lag measurements, the black hole masses, and the velocity-resolved time lags. The discussion of individual objects is in Section 4. Finally, in Section 5, we briefly summarize the present paper.

2. Observations

2.1. Targets

The primary goal of the MAHA project is to monitor the AGNs showing current or historical asymmetric emission-line profiles in order to investigate the BLR geometry and kinematics, their evolution, and the possible presence of SMBBHs. Boroson & Green (1992) adopted the line asymmetry parameter

$$A = \frac{[\lambda_c(3/4) - \lambda_c(1/4)]}{\Delta\lambda(1/2)}, \quad (1)$$

defined by De Robertis (1985), and measured the asymmetries of the Hβ emission lines in PG quasars, where $\lambda_c(3/4)$ and $\lambda_c(1/4)$ are the central wavelengths where the profiles are $3/4$ and $1/4$ of the peak value, respectively, and $\Delta\lambda(1/2)$ is the FWHM of emission line. $A < 0$ indicates that the emission line has a profile with a more pronounced red wing, while $A > 0$ means the line has a stronger blue wing (see Figure 1 in Paper I). Boroson & Green (1992) demonstrated that the A parameter is positively correlated with the relative strength of Fe II with respect to Hβ in PG quasars and some of them have strong asymmetries with $A \lesssim -0.1$ or $A \gtrsim 0.1$. Based on the asymmetry measurements of Boroson & Green (1992), we selected five PG quasars (PG 0947+396, PG 1100+772, PG 1202+281, PG 1310−108, and PG 1613+658) with significant red asymmetries ($A \approx -0.08$ to -0.3) and four PG quasars (PG 1001+054, PG 1048+342, PG 1351+640, and PG 1534+580) with moderate-to-significant blue asymmetries ($A \approx 0.05$–0.15) as our MAHA targets from the PG sample in Boroson & Green (1992). It is intriguing that the Hβ profile of PG 1048+342 has changed to red asymmetry in our observations (see its A parameter measurements from our campaign in Table 1).

We also selected an additional six PG quasars as RM targets: PG 0007+106, PG 0049+171, PG 0923+129, PG 1211+143, PG 1351+695, and PG 1501+106. The radio-emission variability of PG 0007+106 demonstrates quasiperiodicity/periodicity (with a period of ∼5 yr; see Teräsranta et al. 2005; Li et al. 2010), which is potentially caused by jet precession. SMBBHs are a possible cause of jet precession (Begelman et al. 1980; Romero et al. 2000); thus we chose this object as our target. The line profile of PG 1211+143 was almost symmetric in Boroson & Green (1992) but showed mild blue asymmetry recently (see Table 1). PG 1351+695 displayed significant blue asymmetry in 2011 (Barth et al. 2015; Williams et al. 2018). PG 1501+106 showed weak red asymmetry in Boroson & Green (1992); however, this asymmetry became stronger in 2017–2020 (see Table 1). The Hβ emission-line profiles of PG 0049+171 and PG 0923+129 were only weakly asymmetric (Boroson & Green 1992), but we included them in our target list as they fit well into our program schedule (showing stronger red asymmetry in our campaign). Table 1 provides for each target the coordinates, redshifts, asymmetries measured in our campaign (from an individual exposure with a high signal-to-noise (S/N) ratio) and from Boroson & Green (1992), and the specific telescopes used. The mean spectra of our targets are displayed in Figure 1.

2.2. Spectroscopy

The spectroscopic observations were carried out using the 2.3 m telescope of the Wyoming Infrared Observatory (WIRO) in the United States, the Lijiang 2.4 m telescope of the Yunnan Observatories of the Chinese Academy of Sciences in China,

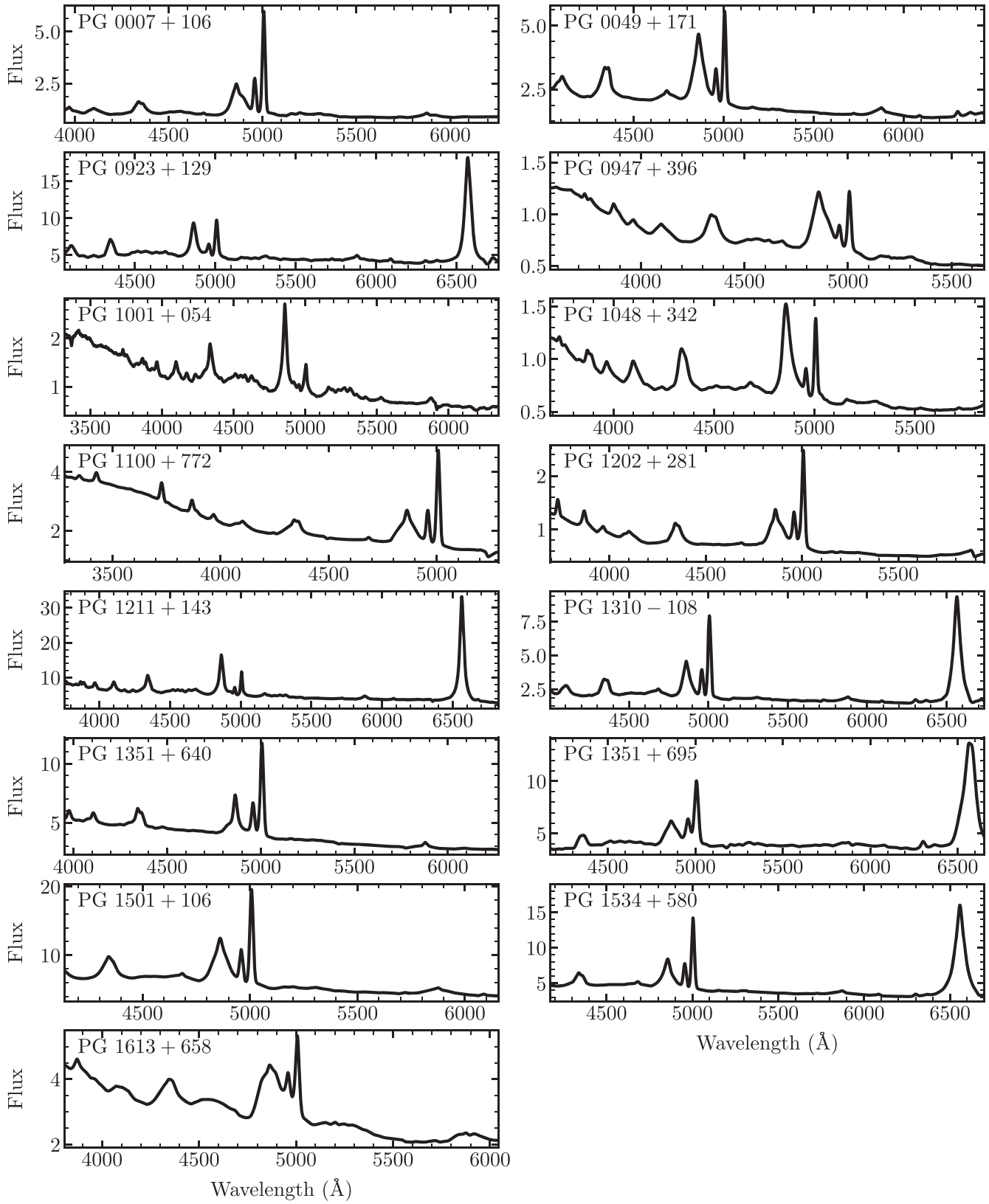

Figure 1. Mean spectra (observed flux density versus rest-frame wavelength) of the objects. Flux units are 10^{-15} erg s^{-1} cm^{-2} Å^{-1}.

the 2.2 m telescope of the Calar Alto Astronomical Observatory of Centro Astronómico Hispano-Alemán (CAHA) in Spain, the Copernico 1.82 m telescope of the Italian National Institute for Astrophysics (INAF) at Mount Ekar in Italy, and the Sutherland 1.9 m telescope at the South African Astronomical Observatory (SAAO) in South Africa. The sites at which individual objects were observed are listed in Table 1. Observations for some objects date back to 2016 December and continued until the northern spring of 2021 for all targets except PG 1211+143 (for which observations concluded in

2017 July). We monitored most of the objects for more than one year. To investigate the potential changes of the BLRs in different years, we usually divided the data for each target into observing seasons bounded by the periods when objects were inaccessible. We did not divide the observations of PG 1100 +772, PG 1351+640, PG 1351+695, PG 1534+580 into segments because the seasonal gaps were small or their variation timescales are too long to get reliable lag measurements from individual seasons (see figures in the following sections). We divided the data of PG 1613+658 into only two seasons because of its relatively long variation timescale. Our observations of PG 0923+129, PG 1211+143, and PG 1310 −108 span only one season. The detailed beginning and end dates, spectroscopic epochs, and cadences for different seasons are listed in Table 3. The spectra obtained from the five telescopes were all reduced using standard procedures (including the corrections of bias and flat field and the wavelength calibration) using IRAF v2.16. Here we briefly introduce the settings of the instruments, apertures, and calibration of the observations at these telescopes.

2.2.1. WIRO Data

We performed RM at WIRO using a 900 l mm^{-1} grating, which provides a dispersion of 1.49 Å $pixel^{-1}$ and a wavelength range of ∼4000–7000 Å. To minimize slit losses and their influence on the flux calibration, a 5″ wide slit oriented north–south was adopted (wider than the typical seeing of ~2″–3″). Spectrophotometric standard stars (usually BD+28°4211, G191B2B, Feige 34, and Hz 44) were used for flux calibration. We used an extraction aperture from −6.″84 to 6.″84, with background windows [−15.″2, −7.″6] and [7.″6, 15.″2] relative to the object's nuclear position. We adopted the [O III]-based technique (e.g., van Groningen & Wanders 1992; Fausnaugh 2017) to perform the relative flux calibration. Where necessary, the spectra of the targets are artificially broadened to achieve the same spectral resolution throughout and then scaled according to their [O III] fluxes (see more details in Paper I). The fiducial [O III] fluxes were determined using the spectra taken in photometric conditions. The [O III] λ4959 lines of PG 1202+281, PG 1351+640, and PG 1351 +695 overlap with their [O III]λ5007 because of their broad line widths (please note that, during the [O III]-based flux calibration, the original spectra were broadened). We used both of the [O III] lines to do the flux calibration in these cases.

During each night, we took three to four consecutive exposures in order to both improve the S/N ratios and evaluate the calibration accuracy by checking their differences. The spectra taken during the same night (after the [O III] calibration) were combined to produce the spectrum for that epoch. In addition to Poisson noise, the difference between the consecutive exposures during the night is caused by the varying weather conditions, seeing variations, or tracking variations during the exposures. This systematic uncertainty was estimated by comparing the fluxes of the exposures in a wide range of wavelengths (4740–5125 Å, effectively eliminating the contribution from Poisson noise) and was added to the error of the continuum and emission-line fluxes of the corresponding epoch using quadratic summation (see more details in Paper I).

Table 2
R.A. and Decl. of the Comparison Stars for Spectroscopy of Two Lijiang Targets

Target	$R.A._{comp}$	$Decl._{comp}$
PG 1001+054	10:04:24	+05:15:29
PG 1211+143	12:13:59	+14:05:16

2.2.2. Lijiang Data

We used the Yunnan Faint Object Spectrograph and Camera (YFOSC) installed in the Lijiang 2.4 m telescope, which is an instrument both for low-resolution spectroscopy and imaging. Grism 14 (with a resolution of 1.8 Å $pixel^{-1}$ and a wavelength range of 3800–7200 Å) and a 2.″5-wide slit were adopted in the campaign. The spectra were extracted in an aperture of ±4.″25 around the nuclear position, with background windows [−14.″15, −7.″36] and [7.″36, 14.″15]. The field de-rotator of the telescope makes it easy to rotate the slit accurately; thus we perform the flux calibration by placing a comparison star simultaneously in the slit (Maoz et al. 1990; Kaspi et al. 2000; see more details in Du et al. 2014). The advantage of the comparison-star-based calibration technique is that it can accurately correct for the changes of the wavelength-dependent atmosphere extinction in different nights. The information of the comparison stars are listed in Table 2. The fiducial spectra of the comparison stars were generated from the data in good weather conditions (calibrated by the spectrophotometric standard stars Feige 34 and Hiltner 600). The target spectra were flux-corrected by scaling the comparison stars to standard values. In order to ensure that the comparison stars were not variable during observations, we performed differential photometry using several field stars. The standard deviations of the photometric light curves of the comparison stars are ∼1% and much smaller than the variation amplitudes of the targets, which means that they can be treated as calibration standards. Similar to the WIRO observations, we took two to three consecutive exposures each epoch. We combined them to obtain the individual-night spectra. In addition, we corrected the small wavelength-calibration uncertainties of the spectra according to their [O III] emission lines before producing the light curves.

2.2.3. CAHA Data

Several spectra of PG 1211+143 were taken using the CAHA 2.2 m telescope from 2017 May to August using the Calar Alto Faint Object Spectrograph (CAFOS). We took the spectra using Grism G-200 and a 3.″0-wide long slit. The wavelength coverage is from 4000 to 8000 Å (with a dispersion of 4.47 Å $pixel^{-1}$). The spectra were extracted in an aperture of ±5.″58, with background windows [−23.″85, −6.″30] and [6.″30, 23.″85]. Similar to the observations at Lijiang, we also adopted the comparison-star-based calibration technique. The coordinates of the comparison star are listed in Table 2. The calibration procedures are the same as for the Lijiang data (see Section 2.2.2).

2.2.4. Asiago Data

For PG 0007+106, PG 1100+772, PG 1202+281, and PG 1501+106, some of the data points come from the Asiago 1.82 m telescope. The spectra were taken using the Asiago Faint Object Spectrograph and Camera (AFOSC), which is a focal reducer instrument similar to YFOSC and CAFOS, with a 4.″2 slit. For PG 0007+106 and PG 1501+106, Grism VPH7

was used, with a wavelength coverage of 3200–7000 Å and a dispersion of 2.95 Å pixel^{-1}. For PG 1100+772 and PG 1202+281, Grism VPH6 was used, with a wavelength coverage of 4500 to 10,000 Å with a dispersion of 2.95 Å pixel^{-1}. We also adopted the [O III]-based calibration, similar to that in the WIRO data reduction. We extracted the spectra using a window of ± 30 pixels (corresponding to ±7.″8). The background was determined using the windows [−13″, −6.″76] and [6.″76, 13″] on both sides of the objects.

2.2.5. SAAO Data

We also took spectra using the SAAO 1.9 m telescope for PG 0007+106 and PG 1501+106. The 600 lines mm^{-1} grating and a slit width of 4.″04 were used. The flux calibration was also performed using the [O III]-based technique. More details of the observations and data reduction can be found in Winkler & Paul (2017). We extracted the spectra using a window of ±6 pixels (corresponding to ±8.″16). The background was determined using the windows [−20.″4, −10.″9] and [10.″9, 20.″4] on both sides of the objects.

2.3. Photometry

The YFOSC and CAFOS instruments can also perform imaging observations. For PG 1001+054 and PG 1211+143, we took Johnson *V*-band images and carried out differential photometry for the targets and the in-slit comparison stars using several other stars in the same fields. The purpose was (1) to make sure that the in-slit comparison stars were not variable during our campaign and (2) to check the flux calibration accuracy of the spectroscopic observations. The fluxes of the targets and comparison stars were extracted using circular apertures with radii of 5.″66 and 5.″30 for YFOSC and CAFOS, respectively. The typical exposure times were 20–50 s. For PG 1001+054, the small scatter of the photometric light curve of the comparison star is at the level of ∼1%–2%, which is stable enough for calibrations. While the comparison star of PG 1211+143 is not in the field of view for photometry, the consistency between its photometric and spectroscopic continuum light curves indicates that its comparison star did not vary significantly and our calibration procedures appear accurate.

To improve the cadence and extend the temporal coverage of the continuum light curves, we also employ archival time-domain photometric data from the All-Sky Automated Survey for SuperNovae[24] (ASAS-SN) and the Zwicky Transient Facility[25] (ZTF). The ASAS-SN project (Shappee et al. 2014; Kochanek et al. 2017) started in 2013 to identify transients and variable sources. Objects with magnitudes between 8 mag and 17 mag in the whole sky are monitored. The details of the data reduction are provided in Shappee et al. (2014) and Kochanek et al. (2017). ZTF makes use of the Palomar 48 inch Schmidt telescope and provides high-quality photometric light curves for objects with magnitudes $\lesssim 20$ (Masci et al. 2019). As of 2021 May, there were six data releases in ZTF. We employ the light curves from ASAS-SN (*g* and *V* bands) and ZTF (*g* and *r* bands) to supplement our photometric and spectroscopic continuum light curves. Considering that the scatter in the ASAS-SN light curves is larger than that of our spectroscopic continuum and the ZTF light curves, we adopted the ASAS-SN data only if they can significantly lengthen the continuum light curves or supplement their temporal coverage (PG 0049+171, PG 0923+129, PG 1211+143, PG 1351+695, PG 1501+106, PG 1534+580, and PG 1613+658). Otherwise, the ZTF light curves are used in the present work.

[24] http://www.astronomy.ohio-state.edu/asassn/index.shtml
[25] https://www.ztf.caltech.edu/

3. Analysis

3.1. Mean and rms Spectra

To check the general Hβ profiles, evaluate their variation amplitudes, and investigate their changes in different seasons, we calculated the mean and rms spectra of the objects for the whole campaign as well as for individual seasons (see Figures 2–16) using

$$\bar{F}_\lambda = \frac{1}{N}\sum_{i=1}^{N} F_\lambda^i, \tag{2}$$

and

$$S_\lambda = \left[\frac{1}{N}\sum_{i=1}^{N}(F_\lambda^i - \bar{F}_\lambda)^2\right]^{1/2}, \tag{3}$$

respectively. Here F_λ^i is the *i*th spectrum of the object, and *N* is the number of its spectra. The narrow [O III] emission lines in the rms spectra are extremely weak or negligible compared to the mean spectra of the same objects, which indicates that our calibration procedure works well. Only the [O III] lines in the rms spectrum of PG 1211+143 have some residual signals. This is caused by the variation of spectral resolution in its exposures with different seeing rather than the flux variations of the [O III] lines. We took the spectra at Lijiang/CAHA (see Table 1) and performed the flux calibration based on the comparison star (see Section 2.2.2) for this object. The variable spectral resolution was not corrected. We measure the standard deviation of [O III]λ5007 flux to be ∼3%, which indicates the reliability of our calibration procedures.

The rms spectra of several objects in some seasons only show weak Hβ emission lines or even what appear to be "absorption lines." There are two main reasons for this: (1) the variation amplitudes of the Hβ fluxes in the corresponding periods are significantly smaller than those in other seasons (e.g., Season 4 in PG 0947+396; Season 2 in PG 1202+281 and PG 1501+106; see Figures 5, 9, and 14), and (2) the variations of their Hβ light curves show reverse modulation with respect to the continuum light curves–in other words, the peaks (troughs) of the Hβ fluxes happen to appear during the troughs (peaks) of the continuum fluxes (see, e.g., the light curves of PG 0947+396 in Season 2 and PG 1202+281 in Seasons 1 and 3; in Figures 5 and 9). To check if the contribution from the reverse variations of the continuum can really weaken the emission-line signals in the rms spectra, we subtracted the continuum beneath the Hβ lines, determined from the linear interpolation between two continuum windows on both sides, from each individual spectrum before calculating the rms spectra for those objects in which the rms spectra showed very weak or "absorption-like" Hβ signals. The continuum-cleaned rms spectra of PG 0049+171, PG 0947+396, PG 1202+281, PG 1351+640, and PG 1501+106 are plotted in Figures 3, 5, 9, 12, and 14, respectively. The continuum-cleaned rms spectra have much stronger Hβ emission lines than the original rms spectra, consistent with

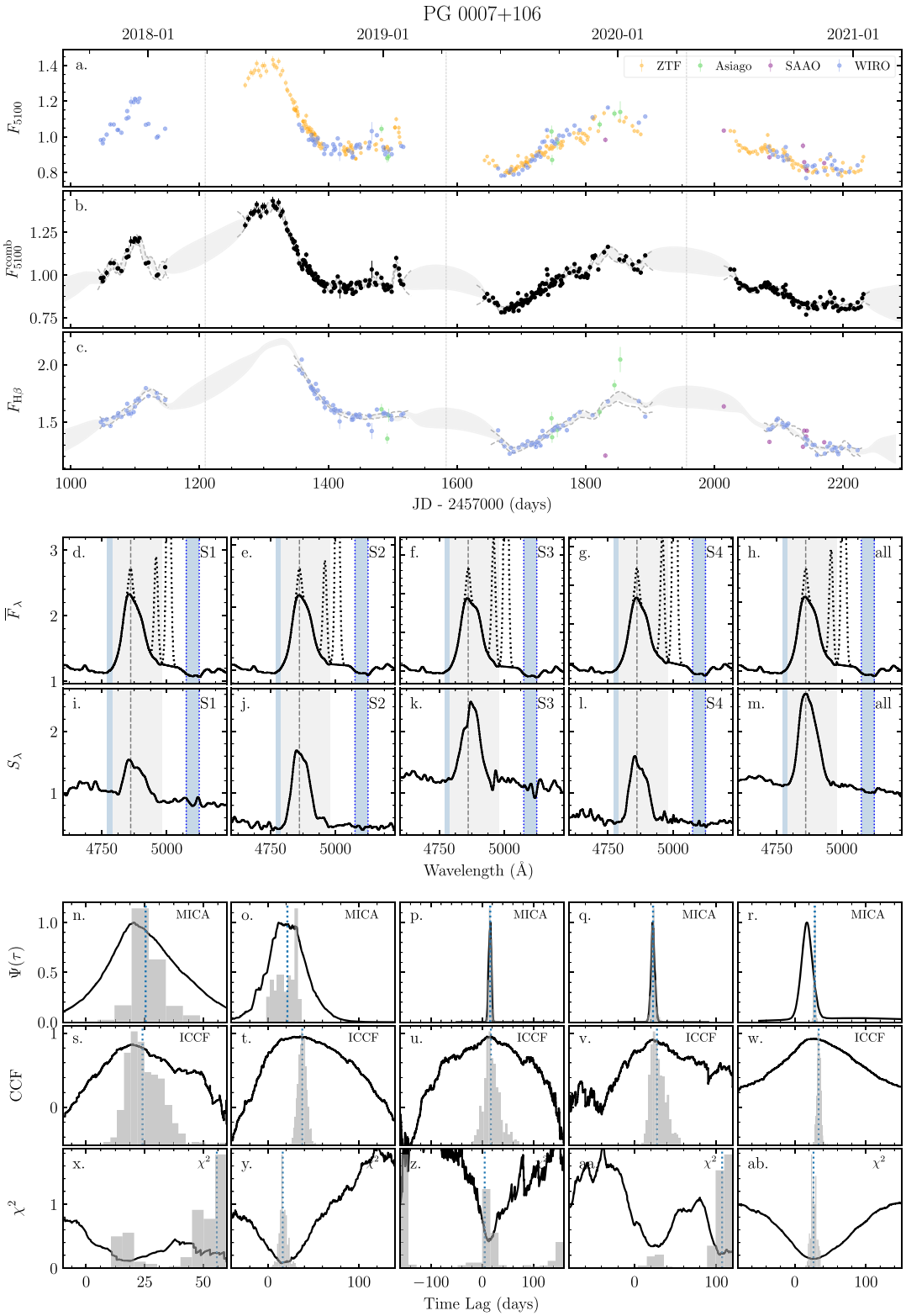

Figure 2. Time-series analysis of PG 0007+106. Panels (a), (b), and (c) are the scaled continuum, combined continuum, and Hβ light curves. The units are 10^{-15} erg s^{-1} cm^{-2} Å^{-1} for panels (a) and (b) and 10^{-13} erg s^{-1} cm^{-2} for panel (c). The gray dotted lines separate different seasons. The gray shadow and gray dashed lines are the MICA reconstructions for the whole light curve and single seasons, respectively. Panels (d)–(m) are the mean (rms) spectra of the seasons and the entire light curve in the rest frames. The black dashed lines are the narrow-line-subtracted mean spectra. The gray and blue shades mark the integration and background windows for Hβ fluxes, and the two blue dotted lines mark the 5100 Å continuum window. The units in panels (d)–(m) are 10^{-15} erg s^{-1} cm^{-2} Å^{-1} (10^{-16} erg s^{-1} cm^{-2} Å^{-1}). Panels (n)–(ab) are the MICA, ICCF, and χ^2 results for the corresponding seasons and the entire light curve (in observed frame). The gray histograms are the distributions of the centroid lags obtained from MICA (CCCDs from ICCF or lag distributions from χ^2 method) in panels (n)–(r), (s)–(w), or (x)–(ab). The blue dotted lines are the median of the distributions. The error bars shown in the light curves do not include the systematic uncertainties in Table 4 (they are used in the time-series analysis in Section 3.5; see also Section 3.2).

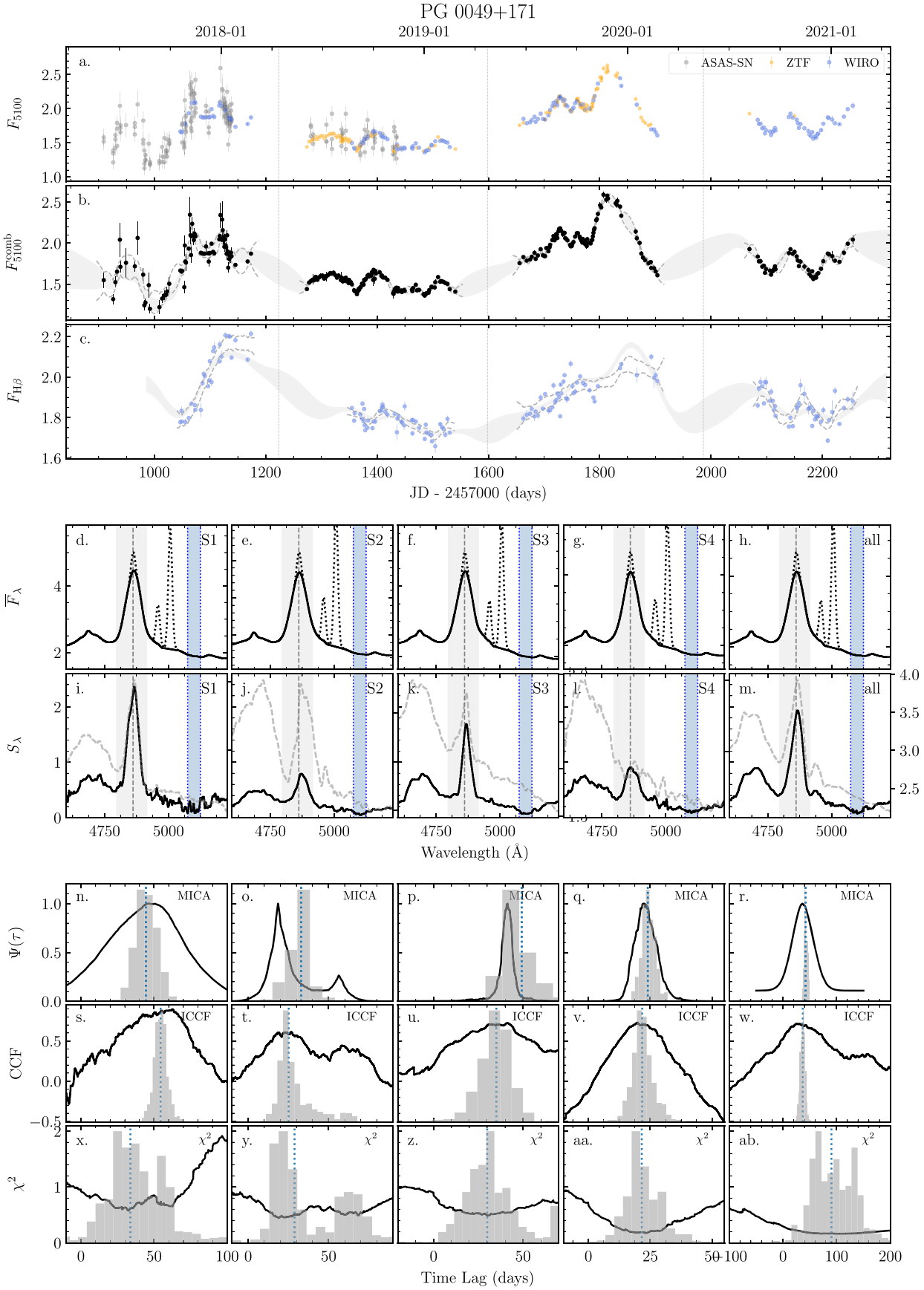

Figure 3. Time-series analysis of PG 0049+171. The gray and black dashed lines in panels (i)–(m) are the original and continuum-cleaned rms spectra (see more details in Section 3.1). The meanings of the other panels, lines, and histograms are the same as in Figure 2.

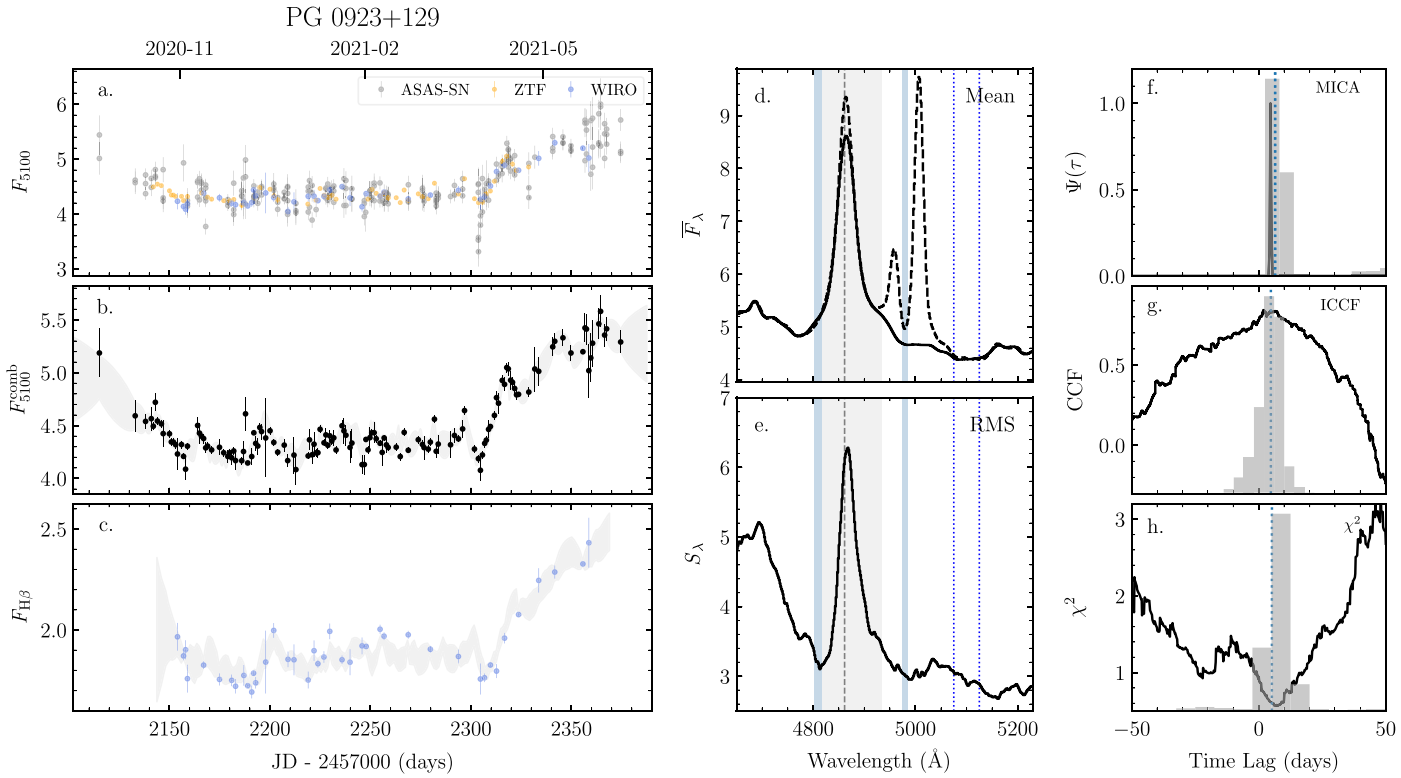

Figure 4. Time-series analysis of PG 0923+129. The meanings of the panels, lines, and histograms are the same as in Figure 2.

the idea that the apparent absorption effect is due the continuum contributions to the emission lines in the rms spectra.

3.2. Light Curves

The Hβ light curves can be measured by the direct integration method (e.g., Peterson et al. 1998; Kaspi et al. 2000; Bentz et al. 2009; Grier et al. 2012; Du et al. 2014) or spectral fitting methods (e.g., Barth et al. 2013; Hu et al. 2015). Paper I has described the advantages and disadvantages of these two methods and explained the reason why we decided to use the direct integration method in our MAHA campaign (see Section 3.1 there). As in Papers I and II, we adopted the integration method to measure the fluxes of the Hβ emission lines. The Hβ fluxes are measured after subtracting the underlying continuum. The continuum and the integration windows are selected according to the emission-line signals in the rms spectra but also to avoid the possible influence of the He II line and [O III] lines as much as possible. The narrow-line fluxes remaining in the integration windows are also included in the Hβ light curves. The 5100 Å continuum light curves are obtained by measuring the median fluxes density from 5075 to 5125 Å. The measurement windows for the continuum and Hβ are marked in the mean and rms spectra in Figures 2–16 for individual objects in different seasons. The light curves are provided in Table 5 and shown in Figures 2–16.

For some objects, the uncertainties described in Section 2 are still smaller than the apparent scatter in the light curves. This indicates that the changes of the weather, pointing, and tracking conditions on different nights have introduced some extra systematic uncertainties. We estimate these systematic uncertainties using the median-filter method (see more details in Du et al. 2014 or Paper I) and are provided in Table 4 as needed. In the following analysis, these systematic uncertainties are also included in the calculations by quadratic summation.

3.3. Intercalibration of Light Curves

Because of the different apertures used for the telescopes in our campaign (as well as ASAS-SN and ZTF) and the correspondingly different contributions from the host galaxies, we need to take care to properly intercalibrate the photometric and spectroscopic light curves. The intercalibration is performed by the Bayesian-based package PyCALI[26] (Li et al. 2014). It assumes that the light curves can be described by a damped random walk model and determines the best multiplicative and additive factors by exploring the posterior probability distribution with a diffusive-nested sampling algorithm (Brewer et al. 2011). The 5100 Å continuum and Hβ light curves from different telescopes are intercalibrated and then combined by averaging the observations during the same nights. The intercalibrated and combined light curves are shown in Figures 2–16. The light curves from different telescopes are generally quite consistent with each other. Several severely deviant data points differing from adjacent epochs and the MICA reconstruction (see below) or possessing significantly larger error bars are not included in the following time-series analysis in Figures 2–16.

In principle, the emission-line contributions (e.g., Hβ, Hγ, He II, Fe II) in the broad bands of photometric light curves may slightly influence the lag measurements. However, the broad-band photometric and spectroscopic (at 5100 Å) continuum light curves are all well consistent with each other in the present paper (see Figures 2–16), which means these influences can be ignored given the current uncertainties of the light

[26] PyCALI is available at: https://github.com/LiyrAstroph/PyCALI.